

Two-Dimensional Model for Polymer-Based Photovoltaic Cells: Numerical Simulations of Morphology Effects

Kristian O. Sylvester-Hvid* and Sten Rettrup†

Department of Chemistry, H. C. Ørsted Institute, University of Copenhagen,
DK-2100 Copenhagen Ø, Denmark

Mark A. Ratner‡

Department of Chemistry, Center for Nanofabrication and Molecular Self-Assembly, and
Materials Research Center, Northwestern University, 2145 Sheridan Road, Illinois 60208-3113

Received: August 19, 2003; In Final Form: December 25, 2003

In this contribution, we develop and investigate a general 2D hopping model for the photovoltaic action in polymer-based thin films. The model takes a microscopic origin and accounts for the molecular photonic and electronic processes by a simple kinetic scheme that eventually leads a linearized master equation for the time evolution of the photovoltaic system. With an emphasis on the topology of blends of donor/acceptor functionalized polymers, we attempt to characterize the dependence of the short-circuit current, internal quantum efficiency, IV characteristics, and fill factors on the morphology of the blend. Several different morphologies for the polymer film are considered, and they show quite different transport and efficiency behavior (e.g., for so-called double cable structures, nearly quantitative conversion efficiencies are computed, and for other structures similar efficiencies may be found, but with short-circuit currents orders of magnitude lower). The model neglects effects such as exciton migration, the built-in potential, and interaction in the third dimension. Nonetheless, significant conclusions can be drawn: in particular, we demonstrate that a viable photovoltaic system driven only by concentration gradients of charge carriers (no built-in field) is possible.

I. Introduction

Within the past decade, there has been tremendous interest in photovoltaic (PV) cells based on thin polymer films as the photoactive component.¹ In terms of cost and practicality for large-scale production, one must distinguish polymer PV cells from organic PV cells in general. Whereas the latter often rely on either highly purified crystals, liquid crystals, or amorphous films deposited under high-vacuum conditions, polymer-based cells offer simple fabrication techniques (i.e., photoactive and semiconducting polymers are deposited either by spin coating or doctor blading onto a substrate from an appropriate organic solvent). This, however, has a profound impact on the morphological properties of the polymer film, which can attain anything from a self-organized to a totally disordered structure.

This study is concerned with developing a theoretical and numerical model for polymer PV devices composed of binary mixtures of p- and n-type polymers, with one or both polymers photoactive. The components may be oligomers—one component may even be single molecules—as long as the overall phase maintains the material properties of a disordered polymer system. At the core of such a model must be the ability to deal with the morphological aspects of such blends. We adopt a molecular picture and represent the electrooptical properties of the p- and n-type polymers in terms of their electron-donating (D) and electron-accepting (A) moieties, respectively.

Since the independent introduction of the bulk-heterojunction concept for polymer blend PV devices by Halls et al.² and Yu

and Heeger,³ the issue of morphology for binary polymer blends with large dispersed internal surfaces has been extensively studied. The rationale behind phase-segregated interpenetrating networks of p- and n-type polymers is the tremendous increase in the DA interface-area-to-volume ratio (roughness factor). The highly convoluted interface is the only effective source of a chemical potential gradient ($\nabla\mu$) capable of driving charge separation (CS) in polymer-blend PV devices. In particular, this is the case because of low dielectric constants resulting in the strong Coulombic binding (0.3–0.7 eV) of photoinduced e^-/h^+ pairs (excitons). By increasing the roughness factor, the average distance that excitons (created within either polymer phase) must travel before encountering a DA interface can be decreased to match the exciton diffusion length while effectively maintaining the optical path length of the device. Additionally, electrons and holes can remain in separate domains, limiting recombination to the DA interface. The conceptual simplicity of bicontinuous DA networks, however, does not match experimental reality, and efficiencies are still limited to below $\sim 2.5\%$ for bulk-heterojunction devices under so-called AM 1.5 conditions.⁴ Also, the anticipated improvements (based on the mere increase in the DA interface area) relative to the corresponding heterojunction devices are lacking, with efficiencies reaching $\sim 1.4\%$ ⁵ in the latter case. A further stark contrast is seen in the near-quantitative yields observed for photoinduced electron-transfer (ET) processes in at least some DA systems⁶ employed in polymer-blend devices. A certain consensus has emerged in the literature as to the practical problems with bulk-heterojunction devices and in particular with respect to morphology: Phase segregation does lead to a large internal interface, but the p- and n-type phases are far from perfectly interconnected. This

* Corresponding author. E-mail: ksh@theory.ki.ku.dk, www.sylvesterhvid.dk/kristian.

† E-mail: rettrup@kiku.dk.

‡ E-mail: ratner@chem.northwestern.edu.

results in dead ends for electron and hole conduction paths and thus increased recombination loss. Also, the lack of segregation into separate p- and n-type domains at the very top and bottom of the film (stratification) leads to structures where both polymer domains are in contact with the same electrode. This also introduces undesired recombination pathways.

Extensive work has been devoted to gaining better control of the morphology of the polymer films.^{4,7–16} The general problem remains, however, that one is trying to control a microscopic nonequilibrium phenomenon (segregation into domains upon solvent evaporation) by tuning a single experimental parameter at a time (e.g., the solvent evaporation rate). For purposes of optimizing PV device performance, searching for the optimal morphology in this multidimensional space of experimental parameters is a formidable task, especially because such parameters may be strongly interdependent.

If one could predict morphological characteristics that would optimize PV action for a given choice of p- and n-type photoactive polymers, experimental efforts could be focused on realizing a much smaller spectrum of potentially viable morphologies. One should realize, however, that the notion of an optimal morphology is not universal but in general will depend on the chemical constitution of the p- and n-type polymers. This can be understood within the simple picture of bicontinuous DA networks (assuming no mixing) where an optimal morphology must reflect a situation where CS across the DA interface and charge transport within domains must be maximized while at the same time recombination across the DA interface and within domains must be minimized. Therefore, the ability to model the PV characteristics of a general network of D and A sites (DA topology) will be helpful in assessing those morphological features essential for PV performance.

The intricacy of optimizing the PV performance by manipulating the morphology of the polymer film suggests combining the essential tasks of photoinduced charge-carrier generation, separation, and transport in one and the same polymer; see ref 17 and references therein. This is realized by making the D and A moieties (via D–A dyads) integral parts of the polymer repeat unit. One then has full control of the local DA arrangement as well as the DA mixing ratio. On spin coating the polymer, one may hope that self-organization will align polymer strands (at least to some extent) such that either D or A groups on adjacent strands pack to form elongated microdomains, pictorially referred to as cables. Conceptually, one could think of this approach as a nanoscopic or molecular interpenetrating network where, because of alignment, the p- and n-type microdomains (the cables) have a common and preferred direction. For such systems, however, one must expect the DA topology to be even more decisive for the PV performance because of the close proximity of the electron and hole transporting regions. In designing such polymers, care should therefore be taken first to ensure favorable conditions for the aggregation of strands and subsequently to ensure that the microdomains formed in fact represent the optimal morphology in terms of balancing molecular CT interactions. We conjecture that the modeling of polymer packing and subsequently the PV characteristics of such packing configurations is essential because of the intimate coupling of the chemical structure of the double-cable polymer and the resulting morphology of the photoactive film.

Here we first develop a theoretical model for the PV properties of general 2D networks of D and A sites with particular emphasis on topology effects and mixing ratios. With this, we hope to address some principal and controversial issues

regarding the current understanding of PV action in molecular-based PV devices. Second, we present preliminary results obtained by numerical simulations for simple DA topologies and subsequently try to relate our results to efficiency–morphology trends experimentally observed.

Modeling morphology effects for blend devices has not been attempted before mainly because representing interpenetrating DA networks in 1D is not meaningful.⁴⁹ Using 1D models, however, heterojunction polymer devices have been described. Barker et al. presented a model based on solving the Poisson and continuity equations self-consistently under stationary conditions.¹⁸ In their model, dissociation of excitons occurs within 1 nm of the DA interface, with the transport of the resulting carriers being due to a combination of field and concentration gradients. Using a somewhat similar assumption with an existing model for inorganics devices, Gregg and Hanna qualitatively accounted for the PV effect in heterojunction devices.¹⁹ In particular, Gregg²⁰ pointed out the importance of ($\nabla\mu$) as the driving force for charge transport in systems where the built-in field (V_{bi})²¹ to a large extent is screened out. Also single-layer polymer,²² molecular crystal,²³ and liquid-crystal²⁴ devices have been modeled, the latter case proving that symmetric cells ($V_{bi} = 0$) make for viable PV devices as well. Common to these studies, however, is the more or less macroscopic approach taken. Nelson used a microscopic approach accounting for the recombination dynamics in polymer-blend devices,²⁵ and Staudigel et al. developed a detailed microscopic model for organic LEDs easily adoptable to organic PV devices.²⁶

We use a microscopic/molecular approach accounting for the photogeneration, transport, and recombination of charge carriers through a predefined set of ET processes among D and A sites and the electrode regions. Because charge transport in disordered media is limited by localization on weakly interacting molecular sites, conduction is mediated by incoherent transport. In treating the coupling of the charge carriers with their surroundings, we adopt the formalism of inelastic electron hopping as used by Petrov et al.²⁷ for transport in molecular wires. Although the problem of charge transport through 1D nanostructures under external radiation has recently been solved exactly,²⁸ here we adopt the semiclassical (perturbative) approximation for the interaction with the radiation field. The generally complex nonequilibrium carrier dynamics is treated within a simple kinetic scheme as we limit our model to consider the illuminated device only under steady-state operation. This, and the fact that we (formally) employ a many-particle formalism, allows for a master equation approach. Modeling charge carrier dynamics therefore becomes a matter of solving linear equations rather than resorting to Monte Carlo simulations. A 2D model should allow a qualitative understanding of topological issues pertaining to interpenetrating networks while avoiding the full complexity of a proper 3D treatment. For disordered polymer blends, our microscopic approach cannot model the PV characteristics of the real-sized devices but only some finite part of the blend. Hence, we set up generic DA topologies, and in those particular cases where these reflect the corresponding macroscopic device structures, we can estimate, by appropriate scaling arguments, the current densities.

In this first attempt to describe PV action in photoactive polymer blends, we wish to keep the model as simple as possible. Thus, we neglect many aspects that have been well established and studied in the literature in order to address the question of how little is actually required to account for the PV action in molecular materials.

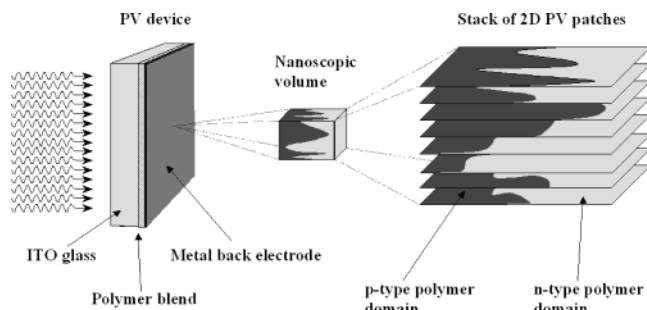


Figure 1. Schematic representation of a PV device composed of a 100-nm-thick photoactive polymer-blend layer sandwiched between front and back electrodes. The nanosized volume is approximated as a distribution of noninteracting 2D patches, each of which subsequently is treated as an individual microscopic PV device.

In section II, we briefly introduce the model and the treatment of charge-carrier dynamics. Section III describes the formalism used to set up and solve the kinetic equations governing the system. Section IV explains the input and the various types of simulations performed, and in section V, we discuss our results. The Appendix gives details regarding the formalism.

II. Model

In Figure 1, we sketch the geometry of a thin-film polymer-based PV device as typically used. The photoactive polymer (blend) is illuminated through a transparent conducting front electrode (usually ITO glass) and interfaced at the back with a metal electrode. In practice, such devices often contain layers of additional components (e.g., PEDOT and LiF are disregarded here). The layer thickness of the photoactive polymer is in the 100-nm range with a total illuminated area of a few cm^2 .

A. 2D Model System. We focus on a nanoscopic volume, say 10^3 nm^3 , of the polymer film, and as illustrated in Figure 1, the composition of this volume represents the local morphology at some sample point in the blend. This volume in turn is considered to be a distribution of 2D PV patches, each of which gives a 2D representation of the actual morphology in the plane of the particular patch. We assume these patches to be noninteracting such that the total photocurrent for the nanoscopic volume is simply the sum of contributions from individual patches.

The 2D morphology for any such patch is discretized as a grid of length A and width B as illustrated in Figure 2b. In this grid representation, which we refer to as the topology, dark squares signify p-type and white squares signify n-type polymer domains. A priori there is no assumption as to the dimension of these squares (referred to as sites), and these may equally well refer to entire domains, individual molecules, or functional groups within polymers, all depending on the desired resolution of the grid. The numbering of sites is given either in coordinate representation (a, b) with $a = 1, 2, \dots, A$ and $b = 1, 2, \dots, B$ or by consecutive numbering with $k = 1, 2, \dots, AB$ as also shown in Figure 2b. We refer to the total number of sites (AB) as K .

Electrodes and external circuitry are formally required, and Figure 2c illustrates how the patch is equipped with a cathode and an anode to form a microscopic 2D photovoltaic device. The electrodes are assumed to be structureless and are characterized only by their ability to donate electrons and holes at certain energies and rates. Also, we assume a bipolar device structure (stratification) such that $a = 1$ sites are p type and $a = A$ sites are n type, as seen in Figure 2c. Apart from introducing electron and hole membranes,²⁹ stratification also simplifies the electrode dynamics considerably.

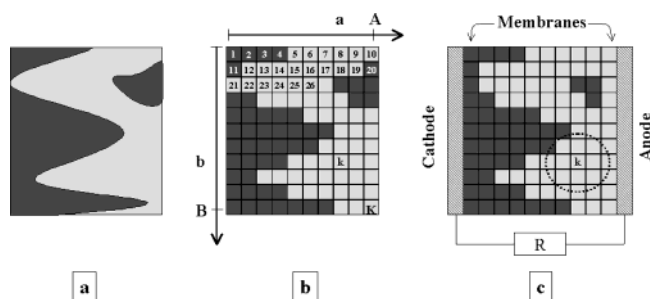


Figure 2. Transition from the 2D representation of the morphology within a 2D PV patch to a virtual microscopic PV device: (a) 2D PV patch representing the p- (dark) and n-type (white) polymer morphologies. (b) Discretized representation of this morphology by a grid A sites long and B sites wide. Sites are either p type (dark) or n type (white) and are numbered consecutively by $k = 1, 2, \dots, K = AB$ or in the coordinate representation as (a, b) . (c) Virtual 2D PV device made by interfacing the PV patch with structureless electrodes and external circuitry. Sites in the first ($a = 1$) and last ($a = N$) columns are entirely p type and n type serving as electron and hole membranes, respectively. The nearest-neighbor hopping sphere around site k is encircled.

Here we specifically adopt a molecular resolution of the grid and assume that the PV characteristics are entirely ruled by the topology and electrochemical nature of the D and A moieties on the p- and n-type polymers, respectively. In fact, we remove any reference to the backbone structure of the polymer strands and focus only on the remaining DA network. Hence, p-type sites contain one D, and n-type sites contain one A functionality. This corresponds to replacing all but the D and A groups with a common dielectric medium.

B. Hopping Dynamics. To illustrate the hopping dynamics of electrons in the illuminated device in Figure 2c, let us begin with the much simpler 1D system ($A = 4, B = 1$) shown in Figure 3a. Each of the four sites $k = 1-4$ is represented in terms of a two-state model with energy levels corresponding to the HOMO and LUMO of the corresponding group (D or A) residing at the particular site. The enumeration of these levels is also given in Figure 3a and generally begins at site $k = 1$ for HOMO levels and continues from $K + 1$ back at site $k = 1$ for LUMO levels, accounting in all for $2K$ levels occupied by an equal number of electrons.

Indicated with filled arrows in Figure 3 are all possible nearest-neighbor ET processes, and with each arrow we associate average forward and backward ET rates. In the hopping regime, electrons are thermally equilibrated at each site such that forward and backward rates can be Boltzmann related. In this way, the device temperature T is introduced into the model.

Three types of hopping processes are displayed in Figure 3a: ET between similar sites occurring either via HOMO or via LUMO levels accounts for hole or electron conduction, respectively. Hopping between unlike sites (D and A) describes ET across the boundary of p- and n-type domains. Finally, polymer-electrode ET here is restricted to occur only between the HOMO on the first D site ($a = 1$) and the cathode and between the LUMO on the last A site ($a = A$) and the anode. More generally, we refer to ET from $a = A$ sites to the anode and ET from the cathode to $a = 1$ sites as injection (electron injection into the anode and hole injection into the cathode). The reverse process (i.e., ET from the anode to $a = A$ sites and ET from $a = 1$ sites to the cathode) is then termed ejection. This nomenclature is exactly opposite of that used for light-emitting diodes where electrons and holes are injected from the electrodes. Under stationary conditions, we require the injection of electrons and holes at the anode and cathode, respectively,

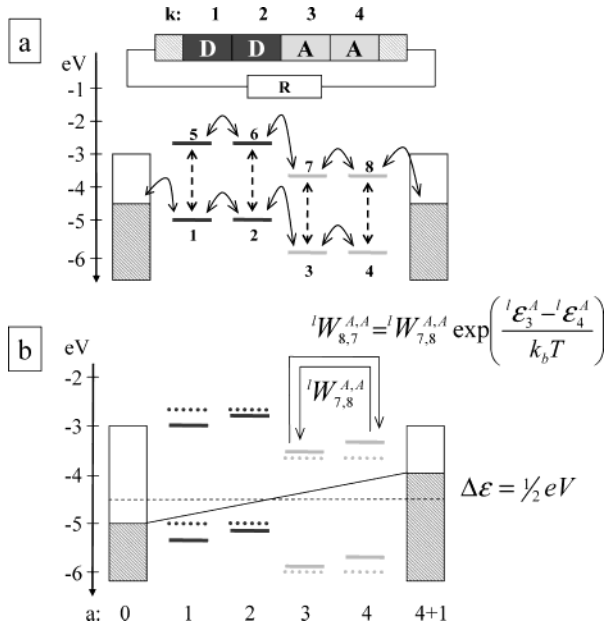


Figure 3. Schematic representation of the M|DDAA|M PV system in terms of HOMO/LUMO levels and Fermi levels of the electrodes. All energies are measured relative to the vacuum level: (a) All included nearest-neighbor hopping processes (arrows shown with solid lines) and photoinduced transitions (arrows shown with broken lines) are under SC conditions and $V_{bi} = 0$. Enumeration of levels begins with HOMO levels {1–4} and continues for LUMO levels {5–8}. (b) Shifting of HOMO/LUMO levels (solid lines) under operating conditions due to a linear potential drop of 1 V across the device. Under biased conditions, up- and downfield transition rates are related by a Boltzmann factor, as illustrated for the LUMO $A \leftrightarrow A$ transition between sites 3 and 4.

to be synchronized such that there is no overall charging of the device. Likewise, the ejection processes are required to be synchronized. In the general case of Figure 2c, an electron injected from the LUMO of any A site with $a = A$ can end up in any HOMO on D sites with $a = 1$ and vice versa for the ejection process. In a primitive fashion, this accounts for the incoherent transport of electrons as they enter the electrode regions.

C. Photoinduced Dynamics. At temperature 0 K and hence in the dark, all 2K electrons occupy the HOMO levels exclusively, whereas at finite T we assume one electron per site free to move about in the system. This redistribution of electrons can occur in any possible way as long as every site is either in a neutral, excited, anionic, or cationic state. As the system is illuminated, optically induced transitions between the HOMO and LUMO on individual sites occur as shown by dashed (vertical) arrows in Figure 3a. The rates for stimulated absorption/emission and spontaneous emission are obtained by approximating each site as a two-state system in equilibrium with unpolarized isotropic radiation of intensity $I(\omega)$. Within the dipole approximation, the rates are³⁰

$$W_{\text{stim}}(\omega) = \frac{2\pi^2 \alpha}{m_e \omega} f(\omega) I(\omega) \quad (1)$$

$$W_{\text{spont}}(\omega) = \frac{2\hbar \alpha \omega^2}{c^2 m_e} f(\omega) \quad (2)$$

where ω is the frequency of the radiation corresponding to the HOMO–LUMO transition with energy gap $\Delta \epsilon = \hbar \omega$. α is the fine-structure constant, m_e is the electron mass, and $f(\omega)$ is the oscillator strength of the transition. The irradiance profile for

terrestrial solar radiation generally has a complicated frequency dependence due to various absorption sources in the atmosphere. In the optical range relevant to PV devices, however, to a first approximation $I(\omega)$ may be given by a Planck expression for a radiating blackbody. Hence, the rates for the optically induced excitation and de-excitation processes at site k are

$$^{\text{ex}}W(k) = \frac{4\pi \Delta \epsilon_k^2}{c^2 \hbar m_e} \alpha f_k \left[\exp\left(\frac{\Delta \epsilon_k}{k_b T_{\text{rad}}(k)}\right) - 1 \right]^{-1} \quad (3)$$

$$^{\text{dex}}W(k) = ^{\text{ex}}W(k) \exp\left(\frac{\Delta \epsilon_k}{k_b T_{\text{rad}}(k)}\right) \quad (4)$$

where $\Delta \epsilon_k$ is the HOMO–LUMO gap and $T_{\text{rad}}(k)$ is the radiation temperature, both at site k . We assume that the radiation intensity is constant throughout the PV patch and that sites with different $\Delta \epsilon$ values see the same radiation temperature. This amounts to setting $T_{\text{rad}}(k) = T_{\text{rad}}$ such that the k dependence in eqs 3 and 4 arises only from variations in $\Delta \epsilon$ and oscillator strengths.

D. Voltage Dependence. We neglect V_{bi} , usually argued to arise from the equilibration of the electrode Fermi levels on assembling the device.³¹ Hence, under short-circuit (SC) conditions ($V = 0$), the situation is as illustrated in Figure 3a where levels for identical sites are degenerate throughout the device (flat-band conditions in band-picture language). In the picture of disorder models for hopping conduction,³² we therefore disregard diagonal disorder. At SC conditions, we further assume that the Fermi level simply is given as the average of the electrode work functions, $\epsilon_0 = \frac{1}{2}(\phi_{\text{anode}} + \phi_{\text{cathode}})$. Asymmetry in terms of carrier diffusion arises, therefore, only by the corresponding asymmetry in the DA topology.

Under operating conditions where power can be extracted, we generally have an electric field along the a axis as a consequence of the potential buildup $V = (\epsilon_L - \epsilon_R)$ between the electrodes. We have chosen a simple linear ramp to model V as justified for polymers with low intrinsic carrier concentrations. Figure 3b displays the symmetric raising (lowering) of cathode (anode) potentials and the shifting of HOMO and LUMO levels in accordance with the linear ramp model

$$\epsilon(a) = \epsilon + \left[\frac{a}{A+1} - \frac{1}{2} \right] \text{ eV} \quad (5)$$

For $a = 0$ and $a = A + 1$ in eq 5, ϵ is taken as ϕ_{cathode} and ϕ_{anode} and thus yields ϵ_L and ϵ_R , respectively. Within the device, ϵ corresponds either to LUMO energies ($l\epsilon^D$, $l\epsilon^A$) or HOMO energies ($h\epsilon^D$, $h\epsilon^A$) for D and A sites, respectively. The electric-field-induced asymmetry necessitates distinction between hopping upfield ($a \rightarrow a + 1$) and downfield ($a \rightarrow a - 1$), and in Figure 3b we show how rates for hopping among similar sites (A sites) then have to be related by a factor $\exp(\Delta \epsilon_{a,a \pm 1}/k_b T)$. Similar considerations apply for the other ET processes.

The V dependence for the injection and ejection rates may result in four distinct situations here referred to as case I–IV. As shown in Figure 4, the values of $\Delta^R \epsilon = \epsilon_R - l\epsilon^A(A)$ and $\Delta^L \epsilon = h\epsilon^D(1) - \epsilon_L$ determine the case that is relevant at a given V . Assuming that under SC conditions $h\epsilon^D < \epsilon_0 < l\epsilon^A$, then in the voltage span between SC and open-circuit (OC) conditions we may in principle encounter the following sequence of cases on increasing V :

$$|\Delta^L \epsilon| < |\Delta^R \epsilon|: \text{ case I} \rightarrow \text{case III} \rightarrow \text{case IV}$$

$$|\Delta^R \epsilon| < |\Delta^L \epsilon|: \text{ case I} \rightarrow \text{case II} \rightarrow \text{case IV}$$

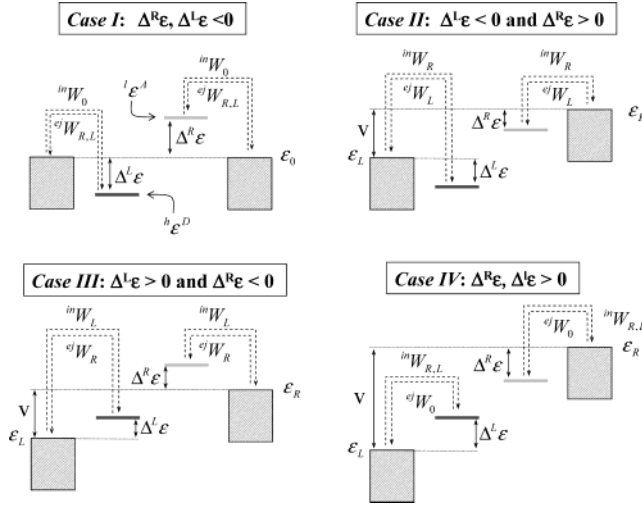


Figure 4. Schematic representation of the four possible injection/ejection situations within the model. In all situations, injection (ejection) processes at the cathode and anode must occur with identical rates because of stationarity. Which rate becomes relevant for a particular process and case is determined by the energy barriers at the cathode ($\Delta^L\epsilon = \hbar\epsilon^D(1 - \epsilon_L)$) and anode ($\Delta^R\epsilon = \epsilon_R - \hbar\epsilon^A(A)$) and ultimately on V and the generic HOMO/LUMO energies. ${}^{\text{in}}W_0$ and ${}^{\text{ej}}W_0$ are the generic (downhill) injection and ejection rates, which are set equal in this study. In case I, ${}^{\text{ej}}W_{R,L}$ designates either ${}^{\text{ej}}W_R$ or ${}^{\text{ej}}W_L$ depending on the relative magnitude of $\Delta^R\epsilon$ and $\Delta^L\epsilon$ and thus on which electrode constitutes the larger ejection barrier. Analogously, in case IV ${}^{\text{in}}W_{R,L}$ designates either ${}^{\text{in}}W_R$ or ${}^{\text{in}}W_L$ depending on which electrode is the larger injection barrier.

TABLE 1: Injection and Ejection Rates for Cases I–IV^a

case	injection barrier	ejection barrier	${}^{\text{in}}W = {}^{\text{in}}W_0 \times$	${}^{\text{ej}}W = {}^{\text{ej}}W_0 \times$
I		$\Delta^{L,R}\epsilon$	1	$\exp(\Delta^{L,R}\epsilon/k_bT)$
II	$\Delta^R\epsilon$	$\Delta^L\epsilon$	$\exp(-\Delta^R\epsilon/k_bT)$	$\exp(\Delta^L\epsilon/k_bT)$
III	$\Delta^L\epsilon$	$\Delta^R\epsilon$	$\exp(-\Delta^L\epsilon/k_bT)$	$\exp(\Delta^R\epsilon/k_bT)$
IV	$\Delta^{L,R}\epsilon$		$\exp(-\Delta^{L,R}\epsilon/k_bT)$	1

^a In cases where both electrodes constitute ejection barriers (case I), the larger one determines the rate, as in cases where both electrodes are injection barriers (case IV). Hence, in cases I and IV $\Delta^{L,R}\epsilon$ signifies either $\Delta^L\epsilon$ or $\Delta^R\epsilon$ depending on which electrode is the barrier.

In each particular case (I to IV), different energy barriers constitute the overall bottleneck for the injection/ejection process as depicted in Figure 4 and as further summarized in Table 1.

III. Methodology

A. Master Equation. We assume that the subsystem is coupled to the surrounding device (the bath) such that thermal equilibrium at the device temperature T prevails throughout and then consider the radiation field to be an additional weak perturbation. We make the approximation that the subsystem and the bath remain in thermal equilibrium even under illumination where work and heat are produced by the subsystem. In this way, we account for the thermalization of electrons in an optically driven system. Symbolically, we may write the Hamiltonian for the entire device as

$$\hat{H} = \sum_k^K \hat{h}(k) + \hat{V}_s \hat{V}_b + \hat{H}_{\text{bath}} \quad (6)$$

where $\hat{h}(k)$ describes an isolated site k (D or A) of the subsystem and where \hat{V}_s contains all mutual couplings among these sites. The surroundings are taken as a bath and are described by \hat{H}_{bath} ,

whereas the coupling of the subsystem and the surroundings is approximated as $\hat{V}_s \hat{V}_b$ with \hat{V}_b depending only on bath variables.

Adopting the Markov approximation for the electron dynamics and assuming weak coupling to the surroundings, it may be argued³³ that the time evolution of the subsystem can be described by the master equation

$$\frac{d}{dt}P(t) = MP(t) \quad (7)$$

where $P_n(t)$ is the probability of finding the subsystem in state $|n\rangle$ at time t and \mathbf{M} is the $N \times N$ transfer matrix, N being the total number of states for the subsystem. The number of electrons is conserved, and the transfer matrix \mathbf{M} takes the usual form with diagonal elements given as

$$M_{mm} = -\sum_{n \neq m} M_{mn} \quad (8)$$

where M_{mn} is the average rate for the subsystem to make the transition $|m\rangle \leftarrow |n\rangle$. Rather than deriving rigorous expressions for these rates, we simply note that³³

$$M_{mn} \propto |\langle m | \hat{V}_s | n \rangle|^2 \quad (9)$$

assuming that states of the entire system are separable into subsystem–bath product states. Using a phenomenological approach, we derive the actual rates by other means (referred to then as W) and use eq 9 only to deduce the structure of \mathbf{M} formally. Our desire to formalize the construction of the transfer matrix stems from the fact that \mathbf{M} depends on the topology of the DA network. Thus, the ability to generate \mathbf{M} efficiently for an arbitrary DA topology is essential for this study.

Because we are not concerned with transient effects, the master equation simplifies to the steady-state result

$$\frac{d}{dt}P(t) = MP(t) = 0 \quad (10)$$

which, subject to the supplementary condition of conservation of probability,

$$\sum_{n=1}^N P_n = 1 \quad 0 \leq P_n \leq 1 \quad (11)$$

may be solved using standard linear algebra tools.

B. Occupation State Space. The subsystem is described by a set of N occupation vectors that form an orthonormal basis $\{|n\rangle\}_{n=1,N}$. Each of these N -particle vectors describes a possible electron occupation configuration of the subsystem and has the form

$$|n\rangle = \underbrace{|O_1^n, O_2^n, \dots, O_p^n, \dots, O_K^n\rangle}_{\text{HOMO levels}}, \underbrace{|O_{K+1}^n, \dots, O_q^n, \dots, O_{2K}^n\rangle}_{\text{LUMO levels}} \quad (12)$$

where the enumeration of levels begins with HOMO levels ($1 \leq p \leq K$) and continues among LUMO levels ($K < q \leq 2K$). Note that index n, m refers to the numbering of states, whereas indices p and q refer to HOMO and LUMO levels, respectively. Because only one electron per site is mobile, we adopt a reduced

representation accounting only for the K active electrons distributed in $2K$ levels.

$$O_p^n = \begin{cases} 1 & \text{doubly occupied HOMO} \\ 0 & \text{singly occupied HOMO} \end{cases} \quad 1 \leq p \leq K$$

$$O_q^n = \begin{cases} 1 & \text{singly occupied LUMO} \\ 0 & \text{vacant LUMO} \end{cases} \quad K < q \leq 2K \quad (13)$$

The representation of the occupation vectors thus becomes analogous to the normal second quantization representation of N -electron states. In the limit of zero temperature where the subsystem attains its single-configuration ground state, only the K HOMO levels are occupied, which defines the reference occupation-state vector

$$|1\rangle = |\underbrace{1, 1, \dots, 1}_K, \underbrace{0, 0, \dots, 0}_K\rangle = \prod_{p=1}^K a_p^\dagger |\text{vac}\rangle \quad (14)$$

where a_p^\dagger creates an electron in level p and $|\text{vac}\rangle$ is the vacuum state. Formally, we may generate the entire state space according to

$$\begin{aligned} \text{single excitations: } a_q^\dagger a_p |1\rangle & \quad n_{\text{ex}} = 1 \\ \text{double excitations: } a_s^\dagger a_t^\dagger a_q^\dagger a_p |1\rangle & \quad n_{\text{ex}} = 2 \\ \dots & \\ \dots & \\ \text{K excitations: } \prod_{k=1}^K a_{q_k}^\dagger a_{p_k} |1\rangle & \quad n_{\text{ex}} = K \end{aligned} \quad (15)$$

where a_p annihilates an electron in level p . From eq 15, we may generate a total of

$$N(K, K) = \frac{(2K)!}{K!K!} \quad (16)$$

states that we may limit choosing $n_{\text{ex}} < K$, reducing the total number of states to

$$N(n_{\text{ex}}, K) = \sum_{i=0}^{n_{\text{ex}}} \left\{ \frac{K!}{(K-i)!i!} \right\}^2 \quad (17)$$

In practice, the state space is generated using the diagrammatic approach outlined in the Appendix, which benefits from a much more compact representation than used here. Also, it allows for the specific generation of a subspace of occupation vectors with only up to n_{ex} excitations out of $|1\rangle$.

C. Constructing the Transfer Matrix. As evident from Figure 2b, the topology of the subsystem is entirely specified by the length (A) and width (B) of the grid along with the topology vector $\mathbf{T} = \{t_1, t_2, \dots, t_k, \dots, t_K\}$, the elements of which are

$$t_k = \begin{cases} A: & \text{if site } k \text{ is acceptor type} \\ D: & \text{if site } k \text{ is donor type} \end{cases} \quad (18)$$

In Figure 2c, the nearest-neighbor coupling sphere for site k is encircled. Among HOMO levels, originating from level p , these couplings are described as

$$(p) \rightarrow \begin{cases} \text{downfield} & \text{sideward} & \text{upfield} \\ (p-1-A) & (p-A) & (p+1-A) \\ (p-1) & & (p+1) \\ (p-1+A) & (p+A) & (p+1+A) \end{cases} \quad (19)$$

and similarly for LUMO levels with q substituted for p . Alternative to the consecutive enumeration of sites, we may use the coordinate representation in terms of (a, b) shown in Figure 2b. To limit the number of indices, we also use (a, b) for the coordinate representation of the HOMO levels such that

$$b(p) = \text{Int}\left[\frac{p-1}{A}\right] + 1$$

$$a(p) = p - [b-1]A \quad (20)$$

with $p = 1, 2, 3, \dots, K$. The corresponding enumeration for LUMO levels is

$$b'(q) = \text{Int}\left[\frac{q-K-1}{A}\right] + 1$$

$$a'(q) = q - K - [b'-1]A \quad (21)$$

where $q = K+1, K+2, \dots, 2K$.

To establish the structure of \mathbf{M} for a given topology (\mathbf{T}), we use the correspondence between M_{nm} and $\langle n | \hat{V}_s | m \rangle$. In this way, we are able to associate with each nonvanishing element of M_{nm} particular hopping events and subsequently assess its numerical value phenomenologically. The coupling operator

$$\hat{V}_s = {}^h\hat{V} + {}^l\hat{V} + {}^c\hat{V} + {}^o\hat{V} \quad (22)$$

operates only within the subsystem state space. The first two terms take the form

$$\begin{aligned} {}^h\hat{V} = \sum_{p=1}^K \{ & \gamma_{1a} ({}^hW_{p-1,p}^{[t_{p-1}, t_p]} a_{p-1}^\dagger a_p + \gamma_{1b} {}^hW_{p-A-1,p}^{[t_{p-A-1}, t_p]} a_{p-A-1}^\dagger a_p \\ & + \gamma_{Bb} {}^hW_{p+A-1,p}^{[t_{p+A-1}, t_p]} a_{p+A-1}^\dagger a_p) + \gamma_{Aa} ({}^hW_{p+1,p}^{[t_{p+1}, t_p]} a_{p+1}^\dagger a_p \\ & + \gamma_{1b} {}^hW_{p-A+1,p}^{[t_{p-A+1}, t_p]} a_{p-A+1}^\dagger a_p + \gamma_{Bb} {}^hW_{p+A+1,p}^{[t_{p+A+1}, t_p]} a_{p+A+1}^\dagger a_p) \\ & + \gamma_{1b} {}^hW_{p-A,p}^{[t_{p-A}, t_p]} a_{p-A}^\dagger a_p + \gamma_{Bb} {}^hW_{p+A,p}^{[t_{p+A}, t_p]} a_{p+A}^\dagger a_p \} \end{aligned} \quad (23)$$

$$\begin{aligned} {}^l\hat{V} = \sum_{q=K+1}^{2K} \{ & \gamma_{1a} ({}^lW_{q-1,q}^{[t_{q-1}, t_q]} a_{q-1}^\dagger a_q + \gamma_{1b'} {}^lW_{q-A-1,q}^{[t_{q-A-1}, t_q]} a_{q-A-1}^\dagger a_q \\ & + \gamma_{Bb'} {}^lW_{q+A-1,q}^{[t_{q+A-1}, t_q]} a_{q+A-1}^\dagger a_q) + \gamma_{Aa'} ({}^lW_{q'+1,q}^{[t_{q'+1}, t_q]} a_{q'+1}^\dagger a_q \\ & + \gamma_{1b'} {}^lW_{q'-A+1,q}^{[t_{q'-A+1}, t_q]} a_{q'-A+1}^\dagger a_q + \gamma_{Bb'} {}^lW_{q'+A+1,q}^{[t_{q'+A+1}, t_q]} a_{q'+A+1}^\dagger a_q) \\ & + \gamma_{1b'} {}^lW_{q'-A,q}^{[t_{q'-A}, t_q]} a_{q'-A}^\dagger a_q + \gamma_{Bb'} {}^lW_{q'+A,q}^{[t_{q'+A}, t_q]} a_{q'+A}^\dagger a_q \} \end{aligned} \quad (24)$$

and account for nearest-neighbor hopping processes among HOMO levels and similarly among LUMO levels. In eq 24, we have used $q' = q - K$ for site indices of topology vector elements and $\gamma_{ij} = 1 - \delta_{ij}$ to eliminate hopping beyond the grid. The third term

$${}^c\hat{V} = \sum_{b,b'=1}^B \{ {}^{ej}W a_{K+bA}^\dagger a_{1+(b'-1)A} + {}^{in}W a_{1+(b-1)A}^\dagger a_{K+b'A} \} \quad (25)$$

accounts for current-generating processes (i.e., the injection of electrons (holes) into the anode (cathode) from the LUMO (HOMO) sites with $a = A$ ($a = 1$) or the ejection of electrons

(holes) from the anode (cathode) into the LUMO (HOMO) sites with $a = A$ ($a = I$). The last contribution in eq 22 describes on-site vertical (optical) transitions between HOMO and LUMO levels

$${}^o\hat{V} = \sum_{p=1}^K \{ {}^{\text{ex}}W^{\dagger}_{p+K} a_p^{\dagger} + {}^{\text{dex}}W^{\dagger}_{p+K} a_p^{\dagger} \} \quad (26)$$

In eq 23–26, we entirely disregard the spin properties of the states. Also, the use of W rather than M emphasizes that the actual rates employed are phenomenological rates. Whether $\langle n | \hat{V}_s | m \rangle$ vanishes or not is simplified by the fact that \hat{V}_s is a one-particle operator connecting only states

$$|n\rangle = a_i^{\dagger} a_j |m\rangle \quad (27)$$

differing in the occupation of levels i and j , where i, j span both HOMO and LUMO levels. The Appendix describes how one specifically generates such pairs of occupation-state vectors using the diagrammatic approach.

D. PV Current, Efficiency, and Average Occupations. Once eq 10 and eq 11 have been solved for \mathbf{P} , we compute the PV current as the net charge-carrier flux resulting from the difference in the injection and ejection flux. The flux contribution from transition $|m\rangle \leftarrow |n\rangle$ is $I_{mn} = \langle m | \hat{I} | n \rangle$, and the current operator is given as

$$\hat{I} = \sum_{b,b'=1}^B \{ {}^{\text{ej}}W a_{K+bA}^{\dagger} a_{1+(b'-1)A} + {}^{\text{in}}W a_{1+(b-1)A}^{\dagger} a_{K+b'A} \} \sum_{n'} P_{n'} |n'\rangle \langle n'| \quad (28)$$

The total PV current is then obtained as

$$I = e \sum_{n \neq m} I_{mn} \quad (29)$$

where the sum may be restricted to all pairs of states differing in the occupation of only two levels.

We may quantify the extent of radiative recombination by evaluating an internal quantum efficiency (IQE), which we define by the ratio of (I/e) to the total number of photons absorbed per time. The latter is evaluated by an expression similar to eq 28, employing only the first term of ${}^o\hat{V}$ in eq 26. Finally, the average site occupancy for site k is found as

$$O_k = \sum_{n=1}^N P_n O_k^n \quad (30)$$

IV. Numerical Simulations

The PV model developed so far requires three types of input: the topology of the DA network, the set of microscopic parameters characterizing the ET dynamics (internal parameters), and external parameters such as radiation and device temperatures along with the voltage across the device. In this first demonstration, our focus is to investigate the extent to which the model can describe effects pertaining to differences in morphology in molecular PV systems. Accordingly, the simulations presented employ the same set of internal and external parameters (but for the voltage), and the DA topology is subject to variations. In applying our model, we refer to the ITO|MDMO-PPV/PCBM|Al³⁴ polymer-blend system because it has been extensively investigated and most of the required parameters can be obtained from the literature.

TABLE 2: ET Rates as Employed in the 2D PV Simulations along with Assumptions by Which These Rates Have Been Obtained

ET process	rates (s ⁻¹)	basis
$D^H \rightarrow D^H$	${}^hW^{DD} = 9 \times 10^5$	eq 31, $l_{DD} = 1.2 \text{ nm}^{46}$ and $\mu_h = 5 \times 10^{-11} \text{ m}^2/\text{Vs}^{47}$
$D^L \rightarrow D^L$	${}^lW^{DD} = 2 \times 10^4$	eq 31, $\mu_e = 10^{-12} \text{ m}^2/\text{Vs}^{48}$ and $l_{DD} = 1.2 \text{ nm}^{46}$
$A^H \rightarrow A^H$	${}^hW^{AA} = 4 \times 10^8$	equal e^- and h^+ mobilities
$A^L \rightarrow A^L$	${}^lW^{AA} = 4 \times 10^8$	eq 31, $l_{DD} = 3.4 \text{ nm}^{36}$ and $\mu_e = 2 \times 10^{-7} \text{ m}^2/\text{Vs}^{36}$
$D^L \rightarrow A^L$	${}^lW^{AD} = 2 \times 10^{13}$	experiment ⁶
$D^H \rightarrow A^H$	${}^hW^{AD} = 1 \times 10^3$	assumption
$A^L \rightarrow A^I$	${}^{\text{in}}W_0 = 1 \times 10^{10}$	assumption
$ITO \rightarrow D^H$	${}^{\text{in}}W_0 = 1 \times 10^{10}$	assumption

A. Internal and External Parameters. The rates for the different ET processes are extracted from experimental data where available, otherwise using qualified estimates. For hopping among similar sites, we derive ET rates from the corresponding electronic mobilities of the pure materials. Writing the diffusion coefficient as $D = Wl^{2,35}$ and the mobility in terms of the Einstein relation $\mu = De/k_bT$, we approximate an average microscopic ET rate as

$$W = \frac{\mu k_b T}{e l^2} \quad (31)$$

which is valid at low internal field strength. In eq 31, l refers to a mean hopping distance for the particular process and can be inferred either from the molecular density or from fitting experimental mobilities to a Gaussian disorder model.³⁶

The rate for hopping from D to A via LUMO levels, ${}^lW^{AD}$, we estimate from time-resolved measurements of photoinduced ET in the MDMO-PPV/PCBM⁶ system. For the corresponding process occurring via HOMO levels, we assume ${}^hW^{AD}$ to be nonvanishing but negligible in comparison. To the best of our knowledge, rates for electron injection/ejection have not been reported for the polymer–electrode combinations addressed here. We therefore choose injection/ejection rates somewhat arbitrarily but sufficiently large so as not to limit the PV efficiency given the present choice of the remaining parameters. In Table 2, we list all hopping rates employed in the simulations and note that if an energy barrier is involved then the rates are listed for the downhill process. For the corresponding reverse processes (uphill), rates are obtained by multiplication with a Boltzmann factor, where $\Delta\epsilon$ is derived from eq 5 and the generic HOMO and LUMO energies as used here are ${}^h\epsilon^D = -5.0 \text{ eV}$, ${}^l\epsilon^D = -2.8 \text{ eV}$ (MDMO–PPV), ${}^l\epsilon^A = -3.7 \text{ eV}$, and ${}^h\epsilon^A = -6.1 \text{ eV}$ (PCBM).³⁴ For cathode and anode work functions, we use $\phi_{\text{ITO}} = 4.7 \text{ eV}^{37}$ and $\phi_{\text{Al}} = 4.3 \text{ eV}^{34}$. Rates for the excitation processes are derived from eqs 3 and 4 and besides site energies require a knowledge of the oscillator strength for the particular site. We assume that D sites have their full absorption potential (i.e., $f_D = 1$), whereas A sites occur with modest absorption corresponding to $f_A = 0.01$. We use a radiation temperature of 1300 K^{38} and a device temperature of 300 K .

B. Computational Details and Size Considerations. The total number of occupation states follows the binomial expression in eq 16, and in the current approach these states, a priori, are equally likely. Thus, prior to solving eqs 10 and 11, there is not a systematic scheme by which we can restrict the state space by sorting out states less important to the PV description. As we move to larger systems and increase K , we must increase n_{ex} accordingly because this is an extensive property of the system, and eventually N becomes infeasibly large

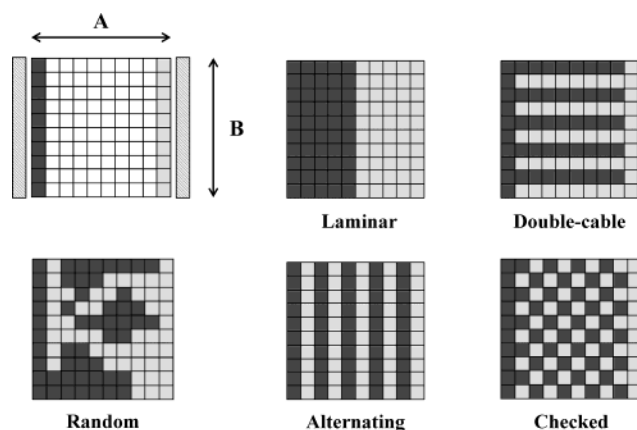


Figure 5. Illustration of the four generic topologies termed laminar, double-cable, alternating, and checked and their orientation relative to the electrodes. Also shown is the 10×10 site structure named random, which serves to exemplify a real device topology in this study.

For a system irradiated with low-intensity radiation such as sunlight, however, highly energetic (multiply excited) occupation states are less likely (i.e., for each additional excitation, the state energy is increased by 2–3 eV). We may therefore argue that as long as the number of sites $K \ll 1/\tau$, τ being the average lifetime of an optical excitation (measured in seconds), setting $n_{\text{ex}} = 1$ can be justified. Consider, for example, a system that is illuminated with AM 1.5 radiation and that fully absorbs, say, in the 550–400-nm range. For the MDMO-PPV/PCBM system in particular, to obtain a number density we must assume that on average a PPV unit (D) and a C_{60} unit (A) each occupy a volume of 1 nm^3 and that DA couples take up the entire volume of the polymer film. Accordingly, a 1-cm^2 polymer film that is 100 nm thick holds on the order of 10^{15} such DA couples. This roughly makes available on the order of 10 eV s^{-1} per site and thus at most 3 excitations/s per site. Assuming that τ is in the range of picoseconds, the duty cycle of the optical transitions in the system is such that for the characteristic size of the systems considered here (≤ 100 sites) $n_{\text{ex}} = 1$ is in fact a very good approximation.

Using $n_{\text{ex}} = 1$ and $K = 100$, we find that a typical simulation involves 10 001 occupation states and that within minutes this may be run using our present simulation code on any desktop computer. With regard to solving the linear equations, we take advantage of the sparse nature of the transfer matrix $\mathbf{M}(\mathbf{T})$, keeping only nonzero elements of \mathbf{M} in memory. But from this we use standard linear equation solvers, and in particular we find the preconditioned biconjugate gradient method³⁹ suitable. Effort, however, has been devoted to the full automation of the generation of $\mathbf{M}(\mathbf{T})$ given any \mathbf{T} and to the efficient handling of the potentially vast number N of occupation-state vectors.

C. Simulations for Different Topologies. The ITO/MDMO-PPV/PCBM/Al devices typically employ an MDMO-PPV/PCBM mixing ratio of 1:4 corresponding roughly to one PPV unit in the p-type polymer to one C_{60} unit in the n-type polymer.^{4,40} Thus, we limit our investigation to generic topologies with a D/A ratio of 1, such as the 10×10 structures shown in Figure 5: The laminar topology is intended to be a 2D model for the ubiquitous bilayered (heterojunction) PV devices, whereas the double-cable topology is intended to be a 2D model for idealized devices consisting of a self-organized double-cable polymer film. Note that the latter topology may also serve as a 2D model for phase-segregated polymer-blend devices if the characteristic domain sizes are in the nanometer range. The alternating topology reflects the situation where a device is

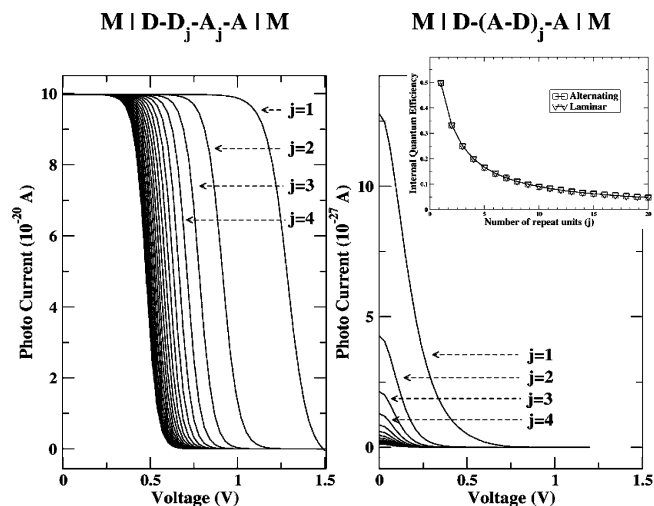


Figure 6. I – V characteristics as simulated for laminar and alternating 1D device structures with the number of repeat units $j = 1, 2, 3, \dots, 20$. The inset shows the computed IQE as a function of j for the structures.

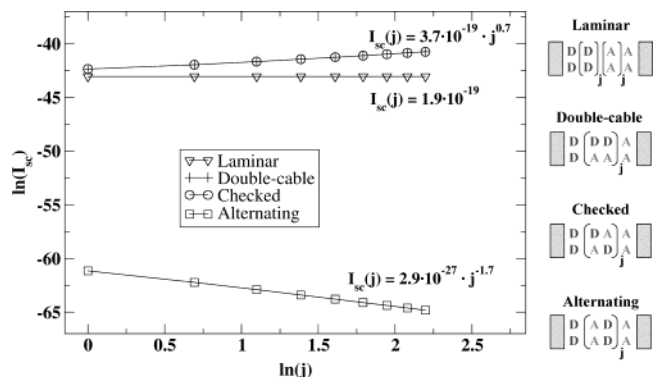


Figure 7. Double-logarithmic representation of $I_{\text{sc}}(j)$ versus length (j) for the four $(2j + 2) \times 2$ structures shown. The power law expressions have been obtained from the linear regression of the data.

imagined to be made from alternating monolayers of D and A, whereas the topology referred to as checked mimics the homogeneous-mixing situation of D and A.

Consider the length dependence of $I(V)$ for the 1D laminar and alternating topologies as shown in Figure 6. Length, as measured by the number j of repeat units, relates to the thickness of the photoactive layer of the device in Figure 2c. In Figure 6, I – V curves have been shown for $j = 1, 2, \dots, 20$ but have been labeled only for $j \leq 4$ because the $(j + 1)$ curve always falls below the corresponding j curve. We observe that $I(V)$ for laminar and alternating structures differs by 7 orders of magnitude and that the shapes of the I – V curves are markedly different. In the alternating case, both the fill factor (FF)⁵⁰ and the open-circuit voltage (V_{oc}) decrease with j and are comparatively smaller than in the laminar case, where in fact it seems that both FF and V_{oc} converge with increasing j . Also, it is clear that I_{sc} decreases with j in the alternating case but is independent of j in the laminar case. The inset in Figure 6 shows the IQE for both topologies as a function of j computed under SC conditions. Surprisingly, both topologies perform with virtually identical IQE despite the huge differences in PV performance.

To simulate the length dependence of I_{sc} for the other topologies, we need to consider structures with $B \geq 2$. Accordingly, for the structures displayed in Figure 7 ($B = 2$) we have simulated I_{sc} for $j = 1, 2, \dots, 10$. On the basis of linear regression, we derive the power-law expressions for $I_{\text{sc}}(j)$ that are also given in Figure 7. We observe virtually identical I_{sc}

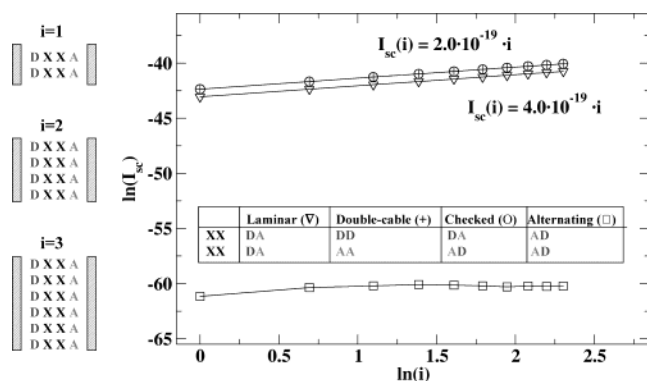


Figure 8. Double-logarithmic representation of $I_{sc}(i)$ versus width (i) for the $4 \times 2i$ structures, the first three of which are shown on the left. For all topologies except the alternating, the linear regression of the data leads to the power law expressions that are also shown.

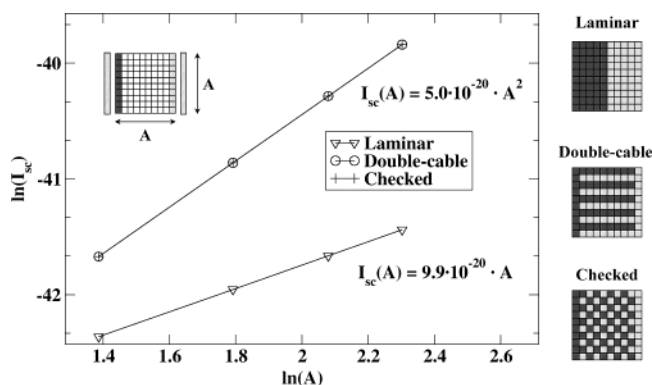


Figure 9. Double-logarithmic representation of $I_{sc}(A)$ versus the side length (A) of the three quadratic structures shown on the right. Power law expressions that are given have been obtained from the linear regression of the data.

for double-cable and checked structures and a near-linear scaling with j . For laminar structures, I_{sc} is independent of j (as in the 1D case in Figure 6), whereas for the alternating structures I_{sc} scales as $j^{-1.7}$.

Figure 8 shows the results for the width dependence of I_{sc} , the width relating to the number i of 2×4 repeat units arranged as illustrated for $i = 1, 2, 3$. Within our 2D model, i therefore scales as the illuminated surface area of the virtual PV device of Figure 2c. Simulations have been performed for $i = 1, 2, \dots, 10$, and by linear regression on data for all but the alternating topology, we find an almost perfect linear scaling of I_{sc} with i . In the alternating case, the data does not fit a simple power expression.

On investigating the scaling of I_{sc} with area of the PV patch, for convenience we consider only quadratic structures with $A = B = 4, 6, 8, 10$ (omitting the alternating topology) as seen in Figure 9. We observe remarkably simple scaling behavior for all three topologies: For the laminar case, we have an almost perfect linear scaling of I_{sc} with A (linear regression yields an exponent of 1.008), whereas for the checked and double-cable cases, quadratic scaling with A is nearly perfect (exponent 1.9996).

V. Discussion

The photocurrents typically obtained in this study may appear unphysically small (on the order of 10^{-20} A), but for the microscopic structures considered they make sense as shown below. In fact, the simulated photocurrents exceed the corresponding dark currents (not shown) by many orders of magni-

TABLE 3: Simulation Results for I_{sc} for Different 10×10 DA Structures All with a D/A Mixing Ratio of 1^a

topology	D/A area	IQE	I_{sc} (A)	J_{sc} (mA/cm ²)
laminar	10	0.20	1.00×10^{-18}	9.8×10^{-6}
double-cable	82	0.99	4.98×10^{-18}	4.9×10^{-4}
checked	152	0.99	4.98×10^{-18}	4.9×10^{-4}
alternating	90	0.20	3.81×10^{-27}	
random	57	0.42	1.84×10^{-26}	

^a For topologies where scaling arguments can be appropriately applied, estimates of the corresponding current densities J_{sc} are given. Also listed are the effective DA interface areas for the different structures.

tude, as expected for intrinsic low-carrier-concentration semiconducting polymers.

Here, as in the simulations, we assume that single PPV units are photoactive, although studies show that at least four or five units are required for absorption in the visible range.⁴¹ Using the number density derived in section 4, we estimate an upper limit to current density J in a situation where all D sites absorb $T_{rad} = 1300$ K radiation with $f_D = 1$ across a HOMO–LUMO gap of 2.2 eV and an IQE of unity. Under such idealized conditions, the optical transitions constitute the overall bottleneck in the system, and each DA couple produces $\sim 0.6 e^-/h^+$ per second: hence J_{max} is on the order 10^{-4} A cm⁻². Polymer devices performing in the 2–3% range give rise to current densities on the order of 10^{-3} A cm⁻².¹ Consequently, our idealized model underestimates the performance of real devices by 1 to 2 orders of magnitude, a discrepancy attributable only to shortcomings in representing the solar intensity and number densities correctly. The failure to reproduce the right order of magnitude for J_{max} is not a source of concern because J displays a very strong dependence on T_{rad} . Thus, within the uncertainty of assessing T_{rad} we could in fact tune T_{rad} such as to make J_{max} the correct order of magnitude. Doing so, however, yields no new insight.

Using the expressions for I_{sc} given in Figure 9, device dimensions as specified above, and assuming devices composed of 100×100 nm patches, we derive J_{sc} as given in Table 3. In the double-cable and checked cases, J_{sc} is comparable to J_{max} but is in fact a bit larger because in the simulation we have $f_A = 0.01$, thus indicating that for these topologies we have close to ideal photoconversion. Within the premises of our 2D model, comparisons of J_{sc} in Table 3 confirm the conjectured as well as experimentally observed⁴² increase in J_{sc} upon changing from a bilayered to an interpenetrating morphology. The actual extent of this increase, here a factor of 50, by no means should be taken to be realistic because conclusions based on 2D modeling may differ significantly from the reality of 3D. We see this trend also at the microscopic level in which I_{sc} scales as the patch area (A^2) in the double-cable and checked cases but only as the DA interface “area” (A) in the laminar case (Figure 9). The close-to-linear scaling of I_{sc} with length for the double-cable and checked topologies in Figure 7 contrasts with the laminar case where I_{sc} is independent of length. We rationalize this by the fact that the DA interface area is independent of length for laminar structures. Because scaling with respect to width is linear in all but the alternating case (Figure 8), the linear scaling in Figure 9 for the laminar case stems solely from the width dependence.

In Table 3, we compare the DA interface area for different topologies (with equal volume), and clearly, in an absolute sense, the area-to-volume ratio does not determine the efficiency because, for example, the alternating and double-cable structures have almost identical interface areas. Only if the basic topologi-

cal features allowing for efficient e^-/h^+ extraction through uninterrupted and directed domains are present does the DA interface area become a relevant parameter. This is the case when making the transition from a laminar to a double-cable topology. The IQE values listed in Table 3 confirm that the double-cable and checked structures exhibit almost quantitative conversion efficiencies. It is noteworthy, however, that the laminar and alternating structures, which differ by 9 orders of magnitude with regard to I_{sc} , show a similar IQE of 20%. This must imply that the alternating structure absorbs considerably less radiation than the laminar structure. In analyzing electron and hole occupancies (not shown here), it becomes clear that the battlement-like arrangement of HOMO levels in alternating structures gives rise to the trapping of holes on D sites and therefore a diminished excitation flux.

Although the simulation of I - V profiles is very dependent on the field model applied, with the linear ramp in eq 5, the simulation of I - V profiles for the alternating and laminar structures still show distinct features as seen in Figure 6. Within the picture of a simple diode model, the I - V curves for laminar structures in Figure 6 are characteristic of a device with high parallel resistance and small series resistance and consequently a large FF. The alternating structures, on the contrary, have I - V curves indicative of small parallel resistance and large series resistance. For both topologies, however, we observe high-voltage behavior suggesting conditions of nonlinear carrier kinetics.

The double-cable and checked structures were intended to mimic different situations, but from simulations, they appear to be identical. However, because we do not distinguish between hopping across a site face or along the diagonal of a site, in terms of the shortest possible conduction paths the topologies are equivalent. Despite the additional conduction paths for the checked structure, both I_{sc} and IQE values in Table 3 are identical for the two structures. Clearly, if the rates were distance-dependent, then the double-cable and checked structures would show different performances. Also shown in Table 3 are results for the structure referred to as random (Figure 5), which are included as a simple illustration of why morphology is essential to polymer-blend devices. This 1:1 blend structure carries features of real (imperfect) bulk heterojunctions: a large dispersed DA interface, variable domain sizes, isolated domains, and conduction paths with a nonuniform distribution of directions. Despite its overall appearance as an interpenetrating network and an IQE ≈ 0.4 , such imperfections lower I_{sc} by orders of magnitude relative to I_{sc} values of the optimal double-cable case.

The topologies in Figure 5 have variable degrees of asymmetry. If terminal sites ($a = 1, A$) are considered separately as hole and electron membranes,²⁹ then in terms of the remaining part of the structure the most efficient topologies are in fact symmetric (i.e., the double-cable and checked structures⁵¹). For these in particular, under SC conditions, the only source of kinetic asymmetry stems from the membranes, yet we have very efficient PV conversion. Hence, our model confirms both the observation²⁴ and simulations¹⁹ by Gregg et al. that systems with $V_{bi} = 0$ can be viable photoconverters. The driving force in our model is the chemical potential gradient $\nabla\mu$ across the DA interface, which, away from SC conditions, is opposed by a V -dependent internal field. More elaborate modeling should allow for $V_{bi} \neq 0$ under SC conditions, which generally would then supplement $\nabla\mu$,²⁰ making our present estimates of I_{sc} a lower limit. However, for polymer-blend devices with a highly convoluted internal interface, one should expect a partial screening out of V_{bi} .

Our simulations clearly show that V_{oc} is determined by the difference in the quasi-Fermi levels (in our simplified model, the electrode potentials) and not (only) by V_{bi} , in accordance with recent studies.^{19,24,43}

Contrary to the simulations by Gregg et al.,¹⁹ we do not limit charge generation to within a small region around the DA interface. In particular for carriers generated away from this interface, the Coulomb binding of e^-/h^+ pairs (exciton binding) is very important. This is not included in our model; consequently, we overestimate bulk charge-carrier generation. Ignoring exciton binding is a shortcoming of our approach, but to some extent it may be compensated by our neglect of energy transfer (i.e., the diffusion of these excitations generated in the bulk to the DA interface). Finally, we have not considered the important nonradiative recombinations here because this requires a knowledge of aspects ranging from vibrational relaxation processes to impurity levels and various extrinsic charge-trapping mechanisms.

VI. Conclusions

We have developed a theoretical 2D model to study morphology effects in binary thin-film polymer-based solar cells. Its microscopic approach is particularly suited to the study of materials in which the optoelectronic properties are largely derived from individual active sites and their mutual interaction. The steady-state carrier dynamics is described by a linearized master equation approach, and solving sets of linear equations gives the steady-state photocurrent directly. Simulations take as input the DA topology and the external and internal parameters chosen to mimic the ITO|MDMO-PPV/PCBM|Al devices. Analyzing the limiting kinetics of this system indicates a 1-to-2-orders-of-magnitude discrepancy of J with respect to experimental systems, attributable to the simplified description of the solar irradiance profile. Simulations of length, width, and area dependences of I_{sc} for different generic DA topologies allows specific scaling relations to be established. Subsequently, 2D estimates of photocurrent densities for macroscopic devices can be derived. Of the topologies investigated, we observe that interpenetrating DA networks give rise to the most efficient devices, whereas bilayered DA devices are a factor of 50 less efficient. Devices made from alternating D and A monolayers perform extremely poorly. Finally, our results demonstrate that exciton diffusion, conduction through bands, and V_{bi} are not prerequisites for a viable PV device and that V_{oc} is not limited by V_{bi} .

Acknowledgment. K.O.S.-H. is indebted to Carlsbergfondet and the Danish Technical Research Council for financial support and the Danish Centre for Scientific Computing for providing computational resources. K.O.S.-H. also thanks J. C. Hummelen for helpful discussions during the preparation of this work. S.R. acknowledges financial support from the Danish Natural Science Research Council. M.A.R. thanks the Chemistry Division of the NSF and the ONR.

VII. Appendix

A. Diagrammatic Representation and Generation of Occupation States. The diagrammatic approach relies on a more compact nomenclature for occupation states, here referred to as configurations. Maintaining the reduced representation introduced in eq 13 and now accounting only for occupied levels, an arbitrary configuration may be written as

$$\mathbf{o} = [o_1, o_2, o_3, \dots, o_K] \quad (32)$$

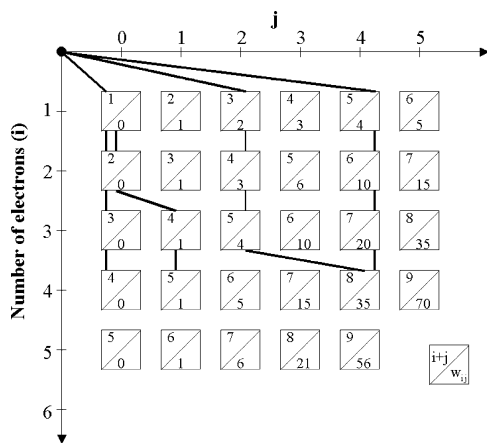


Figure A1. Graphical representation of occupation states. The vertical axis represents an electron number $i = 1, 2, \dots, K$, and the horizontal axis is an auxiliary index $j = 0, 1, \dots, K$. Numbers in the upper triangles are $i + j$ and represent level indices. Occupation states are obtained from allowed paths in the graph, and four distinct states are shown. Lower triangles contain weights w_{ij} used for the dense enumeration of occupation states by means of eq 36.

where entries in the vector \mathbf{o} are indices of occupied levels and where for convenience we have ordered the entries as $o_1 < o_2 < o_3 < \dots < o_K$. The reference state in eq 14 is represented as

$$[1, 2, 3, \dots, p-1, p, p+1, \dots, K-1, K] \quad (33)$$

and similarly the singly excited state

$$[1, 2, 3, \dots, p-1, p+1, \dots, K-1, K, K+q] \quad (34)$$

denotes a configuration where an electron from the p th HOMO is excited into the q th LUMO. To address individual configurations, it is convenient to employ a graphical approach applied in the correlation treatments of many-electron systems.^{44,45} The procedure provides a dense enumeration scheme and a compact indexing of configurations, which then enables an efficient addressing of matrix element contributions. Basically, a given configuration is represented as a path in a very simple and unique graph, as depicted in Figure A1. The vertical axis represents the total number of electrons to be distributed among the $2K$ levels and takes on values of $i = 1, 2, 3, \dots, K$. The horizontal axis indicates a column index of $j = 0, 1, 2, \dots, K$ and is simply an auxiliary index. Consider first the number in the upper triangle of the boxes in Figure A1 as given by $i + j$ and that represents the index of a level. Configurations are assigned a path that always begins at the head (marked with ● in Figure A1) and then is connected to the $(1, j_1)$ box in the line below where $0 \leq j_1 \leq K$. The procedure is continued to the next line by connecting from the selected box in line 1 to a box in line 2, $(2, j_2)$, with $j_1 \leq j_2 \leq K$. This process is continued until the last line K to a box (K, j_K) , $j_{K-1} \leq j_K \leq K$. Clearly, the sequence numbers in the vector $\mathbf{j} = \{j_1, j_2, \dots, j_K\}$ define the path in the diagram where the column indices obey $0 \leq j_1 \leq j_2 \leq \dots \leq j_K$. From a given path, we obtain a configuration \mathbf{o} on setting $o_i = i + j_i$ for $i = 1, 2, 3, \dots, K$.

In Figure A1, we show four distinct paths: $[1, 2, 3, 4]$, $[1, 2, 4, 5]$, $[3, 4, 5, 8]$, and $[5, 6, 7, 8]$ out of 70 possible paths for the system shown in Figure 3a.

To index configurations, we associate with each of the points (i, j) in Figure A1 a so-called weight w_{ij} . The weights for $i = 1$ are given by $w_{1j_1} = j_1$ for $j_1 = 0, 1, 2, 3, \dots, K$, and all weights in the first column are set to zero: $w_{i0} = 0$ for $i = 1, 2, 3, \dots$,

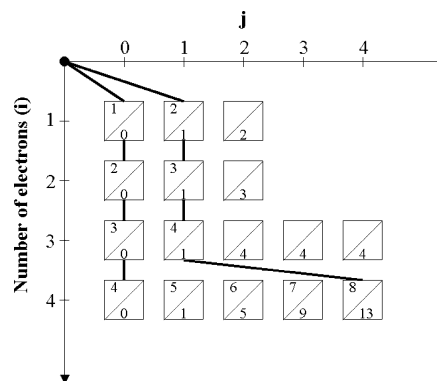


Figure A2. Graphical representation of truncated set of occupation states corresponding to $n_{\text{ex}} < K$. Specific weights associated with $n_{\text{ex}} = 1$ are indicated in the lower triangles. The first and the last paths corresponding to indices 1 and 17 are shown explicitly.

K . The remaining weights in the graph are generated recursively by the relation

$$w_{ij} = w_{ij-1} + w_{i-1j} \quad (35)$$

for $i > 1$ and $j > 0$. The weights are shown in the lower triangles of the boxes in Figure A1, and using these we immediately associate an index with a given configuration (or path). Hence, for configuration \mathbf{o} the index is

$$I(\mathbf{o}) = 1 + \sum_{i=1}^K w_{ij_i} \quad (36)$$

In the above example, we therefore obtain the following indexing: $I([1, 2, 3, 4]) = 1$, $I([1, 2, 4, 5]) = 3$, $I([3, 4, 5, 8]) = 45$, and $I([5, 6, 7, 8]) = 70$. Observe that the reference configuration $([1, 2, 3, 4])$ appears with index 1 and that the all-excited configuration $([5, 6, 7, 8])$ appears with index 70, as equal to the total number of configurations. This is a general characteristic of the dense enumeration scheme employed.

B. Truncated Sets of Configurations. We may wish to limit n_{ex} and thus to generate the subspace of configurations for $n_{\text{ex}} < K$ only. We illustrate here the simplest case where the configuration space is restricted to $n_{\text{ex}} = 1$. For the system in Figure 3a, we identify these configurations from Figure A1 as described above but now with the supplementary conditions that $0 \leq j_i \leq 1$ for $1 \leq i \leq K-1$ and $0 \leq j_K \leq K$. The weights as employed for the complete set ($n_{\text{ex}} = K$) in Figure A1 cannot be applied in the present case because the enumeration will not be dense. This is solved if at the beginning of the calculations of the weights, in addition to the previous definitions, in row 1 and column 0, we set $w_{ij} = 0$ for $1 \leq i \leq K-2$ and $3 \leq j \leq K$. The remaining weights are subsequently calculated recursively using eq 35 as before, and the index is calculated using eq 36. This is illustrated in Figure A2, where the reference configuration $[1, 2, 3, 4]$ still has index 1 but $[2, 3, 4, 8]$ gets index $I([2, 3, 4, 8]) = 1 + 1 + 1 + 1 + 13 = 17$.

C. Localization of Nonzero Transfer-Matrix Elements. To illustrate how we specifically generate pairs of configurations that differ in the occupation of only two levels, consider Figure A3, which is an extension of Figure A1 displaying only $i + j$. To find all pairs of configurations that are different in levels 4 and 10, consider the points with $(i, j) = (3, 1)$ and $(i, j) = (7, 3)$ encircled in Figure A3. It is convenient to decompose the configurations as

$$\mathbf{o} = [o_A \ 4o_B \ o_C] \quad \mathbf{o}' = [o_A \ o_B \ 10o_C] \quad (37)$$

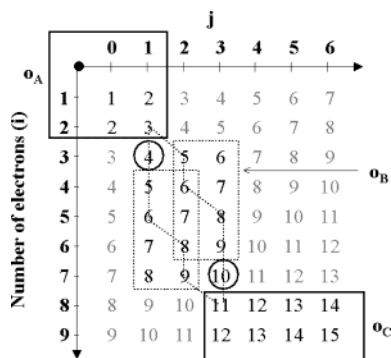


Figure A3. Graphical representation of two occupation states $\mathbf{o} = [o_A \ o_B \ o_C]$ and $\mathbf{o}' = [o_A \ o_B \ 10o_C]$, which differ only in the occupation of levels 4 and 10.

As illustrated in Figure A3, regions o_A and o_C have been framed with solid lines, and the intervening blocks (o_B) have been framed with a dotted line. To generate the configurations, in eq 37 we loop over all possible paths within the o_A and o_C blocks where the paths for each configuration must be equal. The difference in the configurations then occurs only within the o_B region. From Figure A3, it is clear that on generating \mathbf{o} one must follow the lower path and the upper path for \mathbf{o}' as one enters the o_B region. By this method, we then generate all connected pairs of configurations corresponding to selected entries 4 and 10 in the graph. Looping over all such entries within the relevant part of the diagram, we can generate all pairs of configurations that are different in the occupation of only two levels.

References and Notes

- (1) Nelson, J. *Curr. Opin. Solid State Mater. Sci.* **2002**, 6, 87.
- (2) Halls, J. J. M.; Walsh, C. A.; Greenham, N. C.; Marseglia, E. A.; Friend, R. H.; Moratti, S. C.; Holmes, A. B. *Nature* **1995**, 376, 498.
- (3) Yu, G.; Heeger, A. J. *J. Appl. Phys.* **1995**, 78, 4510.
- (4) Shaheen, S. E.; Brabec, C. J.; Sariciftci, N. S.; Padinger, F.; Fromherz, T.; Hummelen, J. C. *Appl. Phys. Lett.* **2001**, 78, 841.
- (5) Jenekhe, S. A.; Yi, S. *Appl. Phys. Lett.* **2000**, 77, 2635.
- (6) Brabec, C. J.; Zerza, G.; Cerullo, G.; Silvestri, S. D.; Luzzati, S.; Hummelen, J. C.; Sariciftci, S. *Chem. Phys. Lett.* **2001**, 340, 232.
- (7) Gebeyehu, D.; Brabec, C. J.; Padinger, F.; Fromherz, T.; Hummelen, J. C.; Badt, D.; Schindler, H.; Sariciftci, N. S. *Synth. Met.* **2001**, 118, 1.
- (8) Halls, J. J. M.; Arias, A. C.; Mackenzie, J. D.; Wu, W.; Inbasekaran, M.; Woo, E. P.; Friend, R. H. *Adv. Mater.* **2000**, 12, 498.
- (9) Arias, A. C.; Mackenzie, J. D.; Stevenson, R.; Halls, J. J. M.; Inbasekaran, M.; Woo, E. P.; Richards, D.; Friend, R. H. *Macromolecules* **2001**, 34, 6005.
- (10) Arias, A. C.; Corcoran, N.; Banach, M.; Friend, R. H.; Mackenzie, J. D.; Huck, W. T. S. *Appl. Phys. Lett.* **2002**, 80, 1695.
- (11) Brabec, C. J.; Padinger, F.; Sariciftci, J. C. H. N. S.; Janssen, R. A. J. *Synth. Met.* **1999**, 102, 861.
- (12) Brabec, C. J.; Padinger, F.; Sariciftci, N. S.; Hummelen, J. C. J. *Appl. Phys.* **1999**, 85, 6866.
- (13) Camaioni, N.; Catellani, M.; Luzzati, S.; Migliori, A. *Thin Solid Films* **2002**, 403–404, 489.
- (14) Chen, L.; Godovsky, D.; Inganäs, O.; Hummelen, J. C.; Janssens, R. A. J.; Svensson, M.; Andersson, M. R. *Adv. Mater.* **2000**, 12, 1367.
- (15) Snaith, H. J.; Arias, A. C.; Morteani, A. C.; Silva, C.; Friend, R. H. *Nano Lett.* **2002**, 2, 1353.
- (16) Padinger, F.; Rittberger, R. S.; Sariciftci, N. S. *Adv. Funct. Mater.* **2003**, 13, 85.
- (17) Cravino, A.; Sariciftci, N. S. *J. Mater. Chem.* **2002**, 12, 1931.
- (18) Barker, J. A.; Ramsdale, C. M.; Greenham, N. C. *Phys. Rev. B* **2003**, 67, 75205.
- (19) Gregg, B. A.; Hanna, M. C. *J. Appl. Phys.* **2003**, 93, 3605.
- (20) Gregg, B. A. *J. Phys. Chem. B* **2003**, 107, 4688.
- (21) Malliaras, G. G.; Salem, J. R.; Brock, P. J.; Scott, J. C. *J. Appl. Phys.* **1998**, 84, 1583.
- (22) Loussaief, N.; Hassine, L.; Boutabba, N.; Kouki, F.; Spearman, P.; Garnier, F.; Bouchriha, H. *Synth. Met.* **2002**, 128, 283.
- (23) Ghosh, A. K.; Feng, T. *J. Appl. Phys.* **1978**, 49, 5982.
- (24) Gregg, B. A.; Fox, M. A.; Bard, A. J. *J. Phys. Chem.* **1990**, 94, 1586.
- (25) Nelson, J. *Phys. Rev. B* **2003**, 67, 155209.
- (26) Staudigel, J.; Stöbel, M.; Steuber, F.; Simmerer, J. *J. Appl. Phys.* **1999**, 86, 3895.
- (27) Petrov, E. G.; Hänggi, P. *Phys. Rev. Lett.* **2001**, 86, 2862.
- (28) Camalet, S.; Lehmann, J.; Kohler, S.; Hänggi, P. *Phys. Rev. Lett.* **2003**, 90, 210602.
- (29) Würfel, P. *Physica E* **2002**, 14, 18.
- (30) Bransden, B. H.; Joachain, C. J. *Physics of Atoms and Molecules*; Longman Scientific and Technical: Essex, England, 1992.
- (31) Malinsky, J. E.; Veinot, J. G. C.; Jabbour, G. E.; Shaheen, S. E.; Anderson, J. D.; Richter, P. L. A. G.; Ratner, A. L. B. M. A.; Marks, T. J.; Armstrong, N. R.; Kippelen, B.; Dutta, P.; Peyghambarian, N. *Chem. Mater.* **2001**, 14, 3054.
- (32) Böttger, H.; Bryksin, V. V. *Hopping Conduction in Solids*; VCH: Berlin, 1985.
- (33) Blum, K. *Density Matrix Theory and Applications*; Physics of Atoms and Molecules; Plenum Press: New York, 1981.
- (34) Brabec, C. J.; Sariciftci, N. S.; Hummelen, J. C. *Adv. Funct. Mater.* **2001**, 11, 15.
- (35) Simon, J.; André, J.-J. *Molecular Semiconductors: Photoelectrical Properties and Solar Cells*; Springer-Verlag: Berlin, 1985.
- (36) Mihailescu, V. D.; van Duren, J. K.; Blom, P. W. M.; Hummelen, J. C.; Janssen, R. A. J.; Kroon, J. M.; Rispens, M. T.; Verhees, W. J. H.; Wienk, M. M. *Adv. Funct. Mater.* **2003**, 13, 43.
- (37) Parker, I. D. *J. Appl. Phys.* **1994**, 75, 1656.
- (38) Grätzel, M.; Moser, J.-E. In *Electron Transfer in Chemistry*; Balzani, V., Ed.; Wiley-VCH: Weinheim, Germany, 2001; Vol. 5, p 589.
- (39) Press, W. H.; Vetterling, W. T.; Teukolsky, S. A.; Flannery, B. P. *Numerical Recipes in Fortran 77*; Cambridge University Press: New York, 2001.
- (40) Yu, G.; Gao, J.; Hummelen, J. C.; Wudl, F.; Heeger, A. J. **1995**, 270, 1789.
- (41) Meier, H.; Stalmach, U.; Kolshorn, H. *Appl. Spectrosc.* **1997**, 48, 379.
- (42) Drees, M.; Premaratne, K.; Graupner, W.; Heflin, J. R.; Davis, R. M.; Marciu, D.; Miller, M. *Appl. Phys. Lett.* **2002**, 81, 4607.
- (43) Ramsdale, C. M.; Barker, J. A.; Arias, A. C.; MacKenzie, J. D.; Friend, R. H.; Greenham, N. C. *J. Appl. Phys.* **2002**, 92, 4266.
- (44) Rettrup, S.; Pauncz, R. *Int. J. Quantum Chem.* **1996**, 60, 91.
- (45) Sarma, C. R.; Palmieri, P.; Rettrup, S. *Mol. Phys.* **2000**, 98, 1851.
- (46) Martens, H. C. F.; Blom, P. W. M.; Schoo, H. F. M. *Phys. Rev. B* **2000**, 61, 7489.
- (47) Blom, P. W. M.; de Jong, M. J. M.; van Munster, M. G. *Phys. Rev. B* **1997**, 55, R656.
- (48) Bozano, L.; Carter, S. A.; Scott, J. C.; Malliaras, G. G.; Brock, P. J. *Appl. Phys. Lett.* **1999**, 74, 1132.
- (49) Work with 2D modeling is currently being undertaken by J. Nelson at the Imperial College of Science
- (50) The fill factor is defined by the ratio $I_{pp}V_{pp}/I_{sc}V_{oc}$, where I_{pp} and V_{pp} are the photocurrent and photovoltage, respectively, at the point of maximum power.
- (51) The checked 10×10 site structure is not symmetric in a rigorous sense. With increasing size, however, the topology approaches a symmetric situation.